

Emergence of Topological Electronic Crystals in Bilayer Graphene–Mott Insulator Heterostructures

Wangqian Miao,¹ Tianyu Qiao,¹ Xue-Yang Song,¹ Yinghai Xu,² Yiwei Chen,² Lei Wang,^{2,3} and Xi Dai¹

¹*Department of Physics, The Hong Kong University of Science and Technology, Clear Water Bay, Hong Kong, China*

²*National Laboratory of Solid-State Microstructures,*

School of Physics, Nanjing University, Nanjing, 210093, China

³*Jiangsu Physical Science Research Center, Nanjing, 210093, China*

(Dated: January 1, 2026)

We predict a new class of topological electronic crystals in bilayer graphene–Mott insulator heterostructures. Interlayer charge transfer creates a charge neutral electron–hole bilayer, in which itinerant carriers in graphene interact attractively with localized carriers from a flat Hubbard band. In the heavy fermion limit and dilute limit, this interplay leads to symmetry breaking crystalline phases stabilized not only by pure repulsion, but also by interlayer Coulomb attraction shaped by band topology. Using comprehensive Hartree Fock calculations, we uncover triangular, honeycomb, and kagome charge orders hosting different quantized anomalous Hall effects at moderate interlayer attraction.

Introduction. A dilute electron gas can spontaneously crystallize due to long range Coulomb repulsion, forming a Wigner crystal [1–3]. When the underlying electronic system hosts nontrivial band topology, such crystallization may give rise to topological electronic crystals, symmetry breaking charge orders that support quantized topological responses [4–9]. These exotic phases have been extensively studied in rhombohedral multi-layer graphene [10–20], where recent experiments have revealed both quantum anomalous Hall (QAH) states and their fractional counterparts [21–23]. These findings underscore the rich interplay between interactions and topological band structures in stabilizing novel crystalline ground states.

Recent experiments [24–26] have shown that correlated insulating phases can also emerge in bilayer graphene (BLG) via long range Coulomb coupling to adjacent charge-ordered systems or patterned dielectric superlattice. Remarkably, such symmetrybreaking phases appear even in the absence of interlayer tunneling or direct hybridization. This raises a natural question: can an interaction-driven topological electronic crystal form spontaneously in BLG without relying on moiré superlattices or engineered periodic potentials [17, 27–31]?

To address this, we consider a bilayer graphene–Mott insulator (BLG–MI) heterostructure in which charge transfer alone generates an interacting electron hole bilayer. The resulting system naturally supports Coulomb coupling between itinerant and localized carriers and enables the emergence of symmetry breaking phases driven by electronic correlations and band topology. As illustrated in Fig. 1(a), the BLG is grounded and placed in contact with a two dimensional Mott insulator multi-layer. In the absence of an applied voltage, charge transfer occurs due to the mismatch in surface work functions: electrons from BLG can diffuse into the unoccupied Hubbard band of the Mott insulator, leaving behind holes in the BLG valence band; alternatively, electrons from the Mott insulator may transfer into BLG, depending on the relative alignment of chemical potentials, as shown in

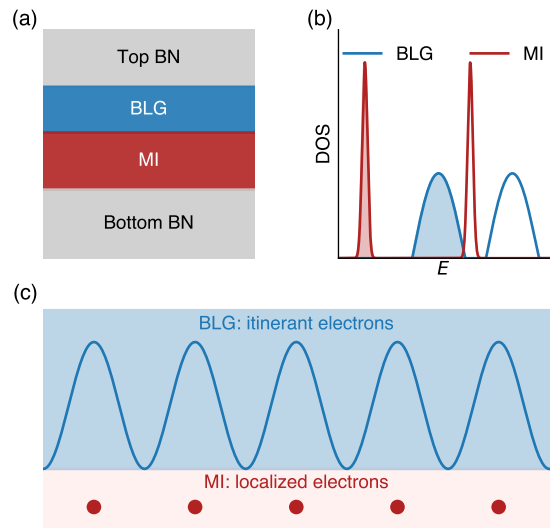


FIG. 1. (a) Schematic of the BLG–Mott insulator heterostructure, encapsulated by boron nitride (BN) layers. (b) Schematic density of states (DOS) of bilayer graphene (BLG) and the Mott insulator (MI), showing energy alignment and charge transfer: the BLG valence band is aligned with the MI upper Hubbard band. Filled regimes indicate occupied states. The band gap opened on BLG is due to displacement field. (c) Real-space depiction of itinerant electrons in BLG (blue curves) and localized electrons in the Mott layer (red dots), illustrating the coexistence of mobile and localized carriers forming an electron–hole bilayer.

Fig. 1(b). This process gives rise to a charge-neutral electron–hole bilayer [32, 33], analogous to carrier redistribution in a conventional *p*–*n* junction. Furthermore, the gate voltage simultaneously controls the electron–hole concentration and the displacement field applied to the

BLG. The Mott layer contributes flat Hubbard bands, hosting heavy and localized carriers akin to f -electrons, while the BLG holes (or electrons) remain light and itinerant, as illustrated in Fig. 1(c). In this Letter, we show that in the heavy fermion limit, a family of electronic crystals forms spontaneously in the dilute regime. These phases exhibit a variety of real-space geometries and host topological orders including the quantum anomalous and spin Hall effects, which may coexist or compete depending on parameters.

Crucially, the electronic crystals we uncover are not stabilized solely by long range repulsion, as in conventional Wigner crystals, but emerge with the interplay of interlayer Coulomb interaction and the nontrivial topology of the BLG bands. Topological bands exhibit an obstruction to constructing exponentially localized Wannier functions [34], reflecting a real space nonlocality of the electronic wavefunctions. This nonlocal structure promotes directional coherence among itinerant carriers, analogous to covalent bonding. In our system, the topology driven bonding tendency is further enhanced by Coulomb interaction, favoring real space patterns beyond triangular order. As a result, the system supports complex charge textures such as honeycomb and kagome crystals. Our results reveal a new organizing principle for electronic crystalline phases, where band topology and interactions cooperate to stabilize symmetry breaking states beyond the Wigner paradigm [35–37].

Model. We begin by establishing the effective Hamiltonian for the BLG–MI bilayer system:

$$H = \sum_{\mathbf{k}} h_c(\mathbf{k}) c_{\mathbf{k}}^\dagger c_{\mathbf{k}} + \sum_{\mathbf{kk}'\mathbf{q}} v_{\mathbf{q}} c_{\mathbf{k}+\mathbf{q}}^\dagger c_{\mathbf{k}'-\mathbf{q}}^\dagger c_{\mathbf{k}'} c_{\mathbf{k}} \\ + \sum_{\mathbf{k}} h_f(\mathbf{k}) f_{\mathbf{k}}^\dagger f_{\mathbf{k}} + \sum_{\mathbf{kk}'\mathbf{q}} v_{\mathbf{q}} f_{\mathbf{k}+\mathbf{q}}^\dagger f_{\mathbf{k}'-\mathbf{q}}^\dagger f_{\mathbf{k}'} f_{\mathbf{k}} \\ - \sum_{\mathbf{kk}'\mathbf{q}} v'_{\mathbf{q}} c_{\mathbf{k}+\mathbf{q}}^\dagger f_{\mathbf{k}'-\mathbf{q}}^\dagger f_{\mathbf{k}'} c_{\mathbf{k}}, \quad (1)$$

where $c_{\mathbf{k}}^\dagger$ ($f_{\mathbf{k}}^\dagger$) creates an itinerant (localized) carrier. The c -electrons are governed by $h_c(\mathbf{k})$, a four-band $\mathbf{k} \cdot \mathbf{p}$ model near the K and K' valleys for each spin, incorporating both layer and sublattice degrees of freedom. The f -electrons originate from the flat upper Hubbard band of the MI surface. $v(\mathbf{q}) = e^2/2S\varepsilon_0\varepsilon_r q$, $v'(\mathbf{q}) = e^2 e^{-qd_0}/2S\varepsilon_0\varepsilon_r q$, where d_0 is the interlayer distance, S is the real space area and $q = |\mathbf{q}|$. This Hamiltonian was previously proposed to study the electron hole bilayer system [38–45] and has a combined $U(1)_c \times U(1)_f$ symmetry which indicates the independent charge conservation in each layer.

In the heavy fermion limit, the kinetic energy of the f -electrons is negligible, and they are treated as static classical variables. This approximation, justified by the extreme flatness of the Hubbard band, enables a Born–Oppenheimer type decoupling [46]: the f -electrons form a fixed background potential for the c -electrons. We then assume the f -electrons form a periodic superlattice that preserves C_{3z} rotational symmetry, with real-space

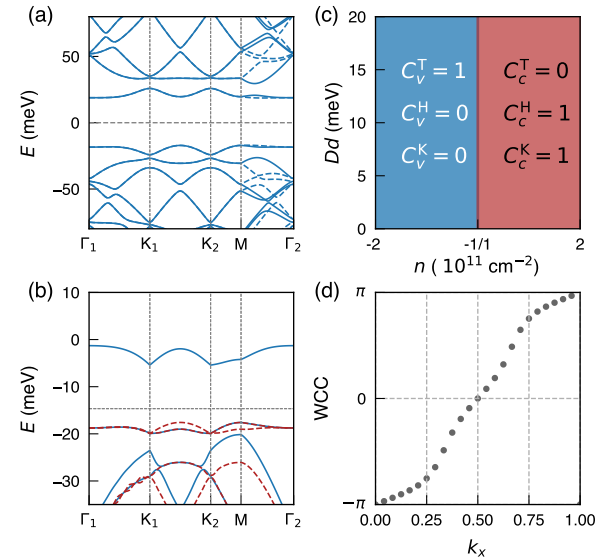


FIG. 2. (a) Single particle band structure of bilayer graphene (BLG) under the superlattice Coulomb potential induced by a triangular arrangement of electrons on the surface of the Mott insulator (MI). Flat bands near the Fermi level are observed. Solid (dashed) lines indicate bands from the K (K') valley. The displacement field Dd on BLG is set to be 20 meV. (b) Self consistent Hartree Fock quasiparticle band structure at one-hole filling per superlattice unit cell, based on the bands in (a). The system forms a spin valley polarized state with a single isolated flat band. Blue (red) lines denote spin up (spin down) bands. (c) Valley Chern numbers C_c and C_v of the first conduction and valence minibands, respectively, for different f -electron superlattice configurations: triangular (T), honeycomb (H), and kagome (K). The variable n denotes the electron–hole pair density; its sign indicates the direction of charge transfer ($n < 0$: electrons transfer from BLG to MI; $n > 0$: reverse). (d) Wilson loop spectrum of the isolated flat band shown in (b), confirming a quantum anomalous Hall insulator with nontrivial topology.

lattice vectors $\mathbf{L}_1, \mathbf{L}_2$. The lattice scale L_s is set by the electron–hole density, which we mainly focus on a very dilute regime at $|n| \approx 10^{-11} \text{ cm}^{-2}$ throughout this work. Note that, the sign for n labels the direction of charge transfer in this Letter. When $n < 0$, the electron transfer from BLG to MI, leaving holes and when $n > 0$, the situation is reversed. The corresponding reciprocal lattice vectors are denoted by \mathbf{G} and \mathbf{Q} . The interlayer Coulomb interaction then simplifies to

$$H_{\text{inter}} = \sum_{\bar{\mathbf{k}}} \sum_{\mathbf{G}, \mathbf{Q}} U(\mathbf{Q}) c_{\bar{\mathbf{k}}, \mathbf{G}}^\dagger c_{\bar{\mathbf{k}}, \mathbf{G} + \mathbf{Q}}, \quad (2)$$

where $\bar{\mathbf{k}}$ lies in the mini Brillouin zone (mBZ), and the effective potential takes the form

$$U(\mathbf{Q}) = - \sum_{\tau} \frac{e^2}{2\varepsilon_0\varepsilon_r\Omega_0} \frac{e^{-|\mathbf{Q}|d_0}}{|\mathbf{Q}|} e^{-i\mathbf{Q} \cdot \boldsymbol{\tau}}. \quad (3)$$

Here, Ω_0 denotes the superlattice unit cell formed by

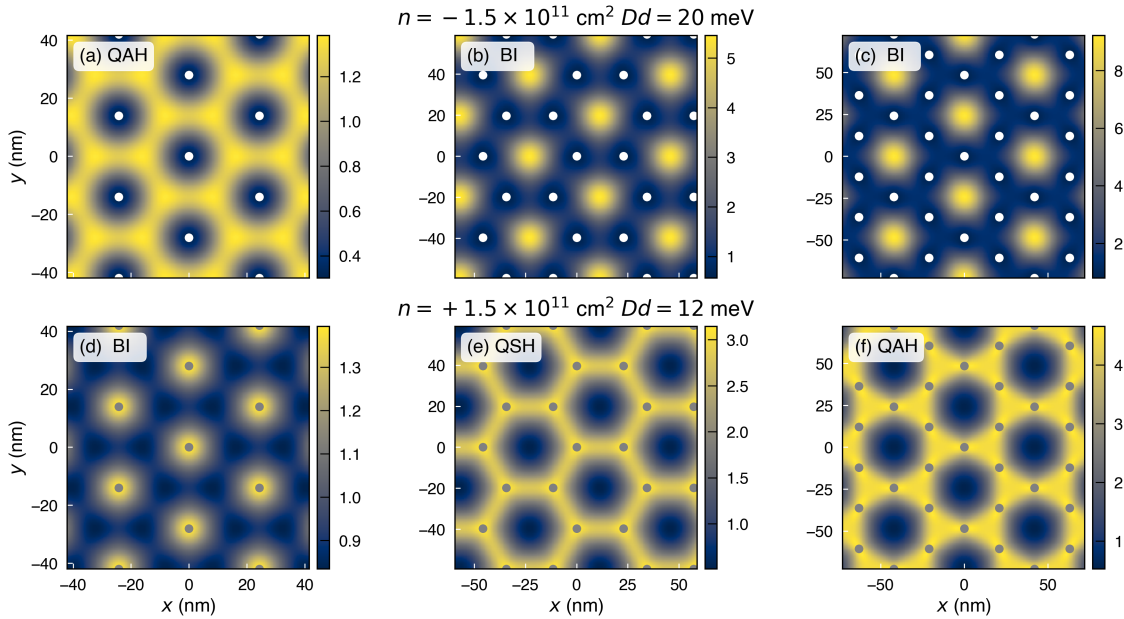


FIG. 3. Real-space carrier density profiles $\rho(\mathbf{r})\Omega_0$ obtained from self-consistent Hartree Fock calculations at fixed total electron–hole density $n = 1.5 \times 10^{11} \text{ cm}^{-2}$. Ω_0 is the unit cell size. White (grey) circles indicate localized electrons (holes) in the Mott insulator (MI). The first row (a–c) corresponds to electrons transferred from BLG to MI ($n < 0$); the second row (d–f) corresponds to electrons transferred from MI to BLG ($n > 0$). (a–c) Electrons on the MI form triangular, honeycomb, and kagome superlattices, leaving one, two, and three holes per unit cell in BLG, respectively. The displacement field on BLG is set to be 20 meV. The resulting states are: (a) a quantum anomalous Hall (QAH) insulator, (b) a band insulator (BI), and (c) another BI. (d–f) Reversed charge transfer, with BLG now hosting the electron crystal. The displacement field on BLG is set to be 12 meV. The resulting topological phases are: (d) BI, (e) quantum spin Hall (QSH) insulator, and (f) QAH insulator.

the f electrons, τ labels the basis positions within this f -electron superlattice, and the structure factor $e^{-i\mathbf{Q}\cdot\tau}$ encodes the geometry of the charge ordering. Different choices of τ define distinct superlattices, such as triangular, honeycomb, or kagome arrangements, each giving rise to a characteristic modulation of the potential $U(\mathbf{Q})$. Further details of the model are provided in the Supplemental Material [47]. This effective Coulomb potential folds the BLG bands into a mini Brillouin zone, opens gaps near the MBZ boundaries, and can in some cases modify the band topology. This mechanism is analogous to recent experimental proposals involving BLG coupled to superlattice patterned gates [27, 28].

Quantum anomalous Hall crystal. We now examine a representative realization of the topological electronic crystal phase. At an electron hole pair density of approximately $|n| \approx 1.5 \times 10^{11} \text{ cm}^{-2}$, the resulting triangular superlattice period is $L_s = 28 \text{ nm}$. We also set $d_0 = 1 \text{ \AA}$ and $\epsilon_r = 10$. In such case, the Coulomb potential generated by f electrons is moderate and can be treated as perturbations. We first consider the case where electrons transfer from the BLG to the Mott insulator, leaving holes in the BLG valence bands. The transferred electrons form a triangular crystal on the MI surface, and the BLG holes experience a periodic Coulomb potential arising from this static charge background.

In this configuration, there is one electron–hole pair

per real space superlattice unit cell. The single particle band structure of the BLG holes under this triangular potential is shown in Fig. 2(a). The interlayer potential folds and flattens the original BLG bands near the K valley, producing nearly flat conduction and valence mini bands per spin and per valley. We find that the first mini conduction band is topologically trivial, while the first mini valence band carries a valley Chern number $C = 1$. This particle–hole asymmetry can be traced to the spatial preference of the carriers: electrons tend to occupy the minima of the superlattice potential, forming a triangular arrangement, whereas holes prefer the potential maxima, which define a honeycomb lattice [28]. The emergence of this effective honeycomb geometry naturally supports nontrivial band topology. Due to the flatness of the mini bands, the system is susceptible to Stoner like instabilities. In particular, a spin valley polarized ground state can emerge, supporting a quantized anomalous Hall effect which is similar to phases observed in other moiré materials. This scenario is confirmed by self-consistent Hartree Fock calculations, where the single particle Green’s function is iteratively updated through the Dyson equation (see Supplementary Material [47]). The resulting mean field quasiparticle band structure is shown in Fig. 2(b), and the Wilson loop for the occupied valence band, plotted in Fig. 2(d), indicates a nontrivial Chern number.

We emphasize that this topological electronic crystal arises only when holes occupy the BLG valence bands. When the charge transfer direction is reversed, electrons are injected into the BLG conduction band, the first mini conduction band is topologically trivial, and the resulting electronic crystal lacks nontrivial topology.

Competing charge orders beyond the triangular lattice.

To explore the broader landscape of electronic crystal phases in the BLG–MI heterostructure, we now consider alternative f -electron arrangements beyond the triangular lattice. Specifically, we study honeycomb and kagome configurations, corresponding to two and three electron–hole pairs per superlattice unit cell, respectively. These geometries are constructed at fixed total electron–hole pair density, ensuring a controlled comparison of competing charge orders.

The interlayer Coulomb potential experienced by the itinerant c -electrons is directly determined by the real space geometry of the f -electron lattice. Compared to the triangular case, honeycomb and kagome arrangements lead to inverted potential profiles: the potential minima form honeycomb or kagome networks, while the maxima lie on triangular sites. This reversal has profound consequences for the resulting band topology and converged charge distribution. In particular, while triangular ordering leads to a topologically nontrivial mini valence band, honeycomb and kagome configurations yield a nontrivial mini conduction band with valley Chern number $C = 1$. This is confirmed by integrating the Berry curvature numerically, with a schematic phase diagram as Fig. 2(c). In the weak potential limit, this band topology can also be understood perturbatively [28, 48], where the superlattice potential modifies the BLG bands without closing the displacement field induced band gap.

For concreteness, we continue to study carrier density $|n| \approx 1.5 \times 10^{11} \text{ cm}^{-2}$. At this fixed density, the superlattice for honeycomb and kagome lattices are around 40 nm and 48 nm, respectively, to maintain the same density of electron–hole pairs. The corresponding single particle band structures are shown in the Supplemental Material [47].

We then perform self consistent Hartree Fock calculations, allowing for spontaneous symmetry breaking. The converged real space charge density $\rho_c(\mathbf{r})$ of the BLG carriers is shown in Fig. 3, alongside the underlying f -electron positions on the MI surface. When $n < 0$, electrons transfer from BLG to the MI and the BLG layer hosts itinerant holes. For triangular f -electron arrangements, the BLG holes form a honeycomb pattern and the system enters a quantum anomalous Hall (QAH) phase. In contrast, if the f -electrons form a honeycomb or kagome lattice, the BLG holes arrange in a triangular pattern and the resulting bands are topologically trivial.

This behavior is reversed when electrons are transferred from the MI to the BLG. In this situation, the BLG electrons organize into honeycomb or kagome patterns under the corresponding f -hole backgrounds, giving rise to nontrivial band topologies, whereas the triangular

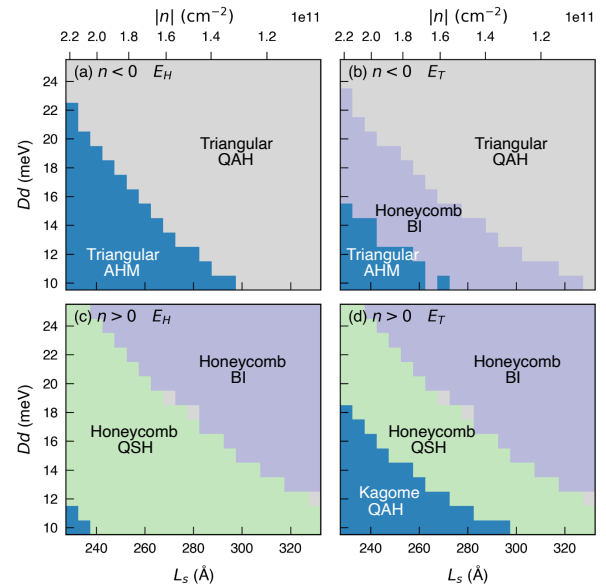


FIG. 4. Phase diagrams of electronic crystals as functions of the electron–hole pair concentration n and displacement field strength Dd , for opposite charge transfer directions. Panels (a,b) correspond to charge transfer from the Mott insulator to BLG, while (c,d) correspond to the reverse direction. The compared energies are (a,c) the Hartree only energy E_H , and (b,d) the total energy including kinetic and Fock contributions, $E_T = E_H + E_{\text{kin}} + E_F$. Colors denote the lowest energy phases, labeled by their lattice geometry and band topology: QAH: quantum anomalous Hall insulator ($C = 1$); QSH: quantum spin Hall insulator ($C_s = 1$); BI: band (correlated) insulator; AHM: anomalous Hall metal. The grey blocks in (c,d) labels metallic honeycomb crystal.

configuration remains topologically trivial. Interestingly, in the honeycomb case, the mean field ground state is a quantum spin Hall insulator, in which two electrons occupy opposite spin–valley flavors ($K \uparrow, K' \downarrow$). In contrast, for the kagome case, three electrons fill three out of the four minibands, realizing a quantum anomalous Hall (QAH) phase. As shown in Fig. 3(e)(f), the real space charge distribution on the BLG layer for these two cases highlights the nonlocal nature of the BLG electrons and their directional bonding tendency.

Ground state and phase diagram. This raises a central question: can these more complex charge orders, which support nontrivial topology, energetically compete with or even surpass the triangular state, despite their less compact real space packing for f electrons? To answer this, we compute the total energy E_T for various superlattice configurations, including the Hartree energy E_H of both itinerant (c) and localized (f) carriers, along with the kinetic E_{kin} and Fock exchange energies E_F of the c electrons in BLG. The Hartree terms capture classical electrostatics, while the latter two incorporate quantum effects arising from the BLG miniband structure. For such electron–hole bilayer, the Hartree energy is calcu-

lated as

$$E_H = \frac{1}{2} \int d\mathbf{r} d\mathbf{r}' \frac{e^2}{4\pi\epsilon_r\epsilon_0|\mathbf{r} - \mathbf{r}'|} (\rho_c(\mathbf{r})\rho_c(\mathbf{r}') + \rho_f(\mathbf{r})\rho_f(\mathbf{r}')) - \int d\mathbf{r} d\mathbf{r}' \frac{e^2}{4\pi\epsilon_r\epsilon_0\sqrt{|\mathbf{r} - \mathbf{r}'|^2 + d_0^2}} \rho_c(\mathbf{r})\rho_f(\mathbf{r}'), \quad (4)$$

where $\rho_f(\mathbf{r}) = \sum_{i,\tau} \delta(\mathbf{r} - \mathbf{R}_i - \boldsymbol{\tau})$ denotes the real space density for f electrons (holes) and \mathbf{R}_i is the lattice vector. To ensure accuracy and consistency, we employ Ewald summation for long-range Coulomb interactions and perform finite-size scaling to eliminate numerical artifacts. As shown in Fig. 5, for the case of $|n| = 1.5 \times 10^{11} \text{ cm}^{-2}$, when $n < 0$ (electrons transferred from BLG to the Mott insulator), the topological triangular phase with Chern number $C = 1$ minimizes the total energy, outperforming the trivial honeycomb and kagome arrangements. In contrast, for $n > 0$ (electrons transferred from the Mott insulator to BLG), the topological honeycomb and kagome phases exhibit lower condensation energies than the triangular lattice. This reversal arises from the interplay between band topology and interlayer Coulomb attraction: the periodic Coulomb potential from the f -electron lattice reshapes the BLG wavefunctions, enabling c electrons in topological minibands to form real space patterns that enhance interlayer attraction. This reorganization optimizes the charge distribution and stabilizes the ground state by lowering down the total Hartree energy. By varying the displacement field Dd and electron hole pair density n , we perform comprehensive Hartree–Fock calculations and construct a phase diagram of the energetically favored charge configurations in Fig. 4. A key finding is the emergence of an extended regime of topological electronic crystals with nontrivial real space geometries beyond the conventional triangular order. For $n < 0$, the triangular configuration minimizes the Hartree energy. However, in certain parameter regimes, the honeycomb band insulator becomes energetically favorable because the larger lattice scale produces flatter bands, which suppress the kinetic energy and consequently reduce the Fock exchange energy. This effect can be understood from the ratio between the Coulomb and kinetic energies, estimated as $\frac{m^* L_s e^2}{\epsilon_r \epsilon_0 \hbar^2}$ which increases with L_s , thereby enhancing interaction driven effects in flatter of honeycomb or kagome configuration. For $n > 0$, the honeycomb and kagome configurations dominate, and a QAH phase emerges in the kagome case near $n \approx -2 \times 10^{11} \text{ cm}^{-2}$, $Dd \approx 12 \text{ meV}$. Increasing the displacement field suppresses the honeycomb QSH phase, driving an interaction induced transition accompanied by a metallic intermediate state. These phases remain stable upon varying the interlayer distance and dielectric constant, as shown in the Supplemental Material [47].

Discussion. The BLG–MI model studied in this Letter can be viewed as a quantum capacitor comprising a layer of classical charges and a layer of quantum particles with a parent topological band structure, in the regime where

$L_s \gg d_0$ and for moderate attractive interaction. Such complex charge textures have no counterpart in a purely classical system. For comparison, one may consider a layer of classical charges periodically arranged beneath a parallel grounded metallic plate at a distance d_0 , forming an overall charge neutral configuration. In this classical limit and dilute regime, the induced charges on the metallic plate will concentrate above the classical charge distribution, forming a Wigner dipole crystal [49] (See Supplemental Material [47] for this classical model). The true ground state in this case is a triangular lattice [50], as shown in Fig. 3(d). In another limit, if the interlayer $f - c$ attraction dominates over the kinetic energy of the c electrons, these carriers bind into dipoles which results in a crossover to a classical description. We also comment on potential material platforms. On the itinerant side, beyond BLG, alternative two dimensional electron gasses (2DEGs) with spinor structures, such as systems exhibiting Rashba spin orbital coupling [51] or quantum wells described by the Bernevig–Hughes–Zhang model [52–55], are promising candidates. On the Mott insulator side, layered two dimensional materials such as CrOCl [24], Nb_3X_8 (X=Cl, Br, I) [56–58] provide possible realizations.

We end this Letter by outlining several directions extend beyond the present mean field treatment. First, we have adopted the heavy fermion limit, treating the f -electrons(holes) as static classical charges. When their effective mass becomes comparable to that of the itinerant carriers, quantum fluctuations must be restored, enabling competing excitonic condensates. Second, while we have focused on symmetry breaking insulators at integer fillings, the topological nature of the mini bands points to the possibility of fractionalized excitations. For instance, in the triangular QAH phase, a single hole may fractionalize across spin valley sectors into paired composite Fermi liquids, potentially realizing non-Abelian or multicomponent fractional Chern insulators beyond the mean field regime [59–64]. Finally, we have mainly considered a charge neutral configuration where a p – n junction forms at the interface of the two materials, although trionic fluids phases may also emerge [65–68].

Note Added. Charge transfer induced heavy Wigner crystal phases have been observed in a recent Letter [69]. Our corresponding experimental paper is in progress [70].

Acknowledgments. W. Miao thanks fruitful discussion with F. Desrocher on the numerics of Hartree Fock calculations. L. Wang acknowledges the support from National Key Projects for Research and Development of China (Grant No. 2022YFA1204700 & 2021YFA1400400), National Natural Science Foundation of China (Grant No. 12525403 & 12550404) and Natural Science Foundation of Jiangsu Province (Grant No. BK20253027 & BK2023300). X.Y. Song is supported by the Early Career Scheme of Hong Kong Research Grant Council (Grant No. 26309524). X. Dai is supported by a fellowship award from Hong Kong Research Grant Council (Project No. SRFS2324-6S01) and New Conerstone

Science Foundation.

Data availability. The data generated by the Hartree

Fock code are publicly available at [data will be made available on Zenodo upon publication].

[1] E. Wigner, On the Interaction of Electrons in Metals, *Phys. Rev.* **46**, 1002 (1934), publisher: American Physical Society.

[2] V. Goldman, M. Santos, M. Shayegan, and J. Cunningham, Evidence for two-dimentional quantum wigner crystal, *Physical review letters* **65**, 2189 (1990).

[3] H. Li, S. Li, E. C. Regan, D. Wang, W. Zhao, S. Kahn, K. Yumigeta, M. Blei, T. Taniguchi, K. Watanabe, *et al.*, Imaging two-dimensional generalized wigner crystals, *Nature* **597**, 650 (2021).

[4] Z. Tešanović, F. m. c. Axel, and B. I. Halperin, “hall crystal” versus wigner crystal, *Phys. Rev. B* **39**, 8525 (1989).

[5] Y. Zeng, D. Guerci, V. Crépel, A. J. Millis, and J. Cano, Sublattice Structure and Topology in Spontaneously Crystallized Electronic States, *Phys. Rev. Lett.* **132**, 236601 (2024), publisher: American Physical Society.

[6] T. Tan and T. Devakul, Parent Berry Curvature and the Ideal Anomalous Hall Crystal, *Phys. Rev. X* **14**, 041040 (2024), publisher: American Physical Society.

[7] T. Soejima, J. Dong, A. Vishwanath, and D. E. Parker, *A Jellium Model for the Anomalous Hall Crystal* (2025), arXiv:2503.12704 [cond-mat].

[8] S. Joy, L. Levitov, and B. Skinner, Chiral wigner crystal phases induced by berry curvature (2025), arXiv:2507.22121.

[9] K.-S. Kim, Magnetic interactions of wigner crystal in magnetic field and berry curvature: Multi-particle tunneling through complex trajectories (2025), arXiv:2508.13149.

[10] J. Dong, T. Wang, T. Wang, T. Soejima, M. P. Zaletel, A. Vishwanath, and D. E. Parker, Anomalous Hall Crystals in Rhombohedral Multilayer Graphene. I. Interaction-Driven Chern Bands and Fractional Quantum Hall States at Zero Magnetic Field, *Phys. Rev. Lett.* **133**, 206503 (2024), publisher: American Physical Society.

[11] T. Soejima, J. Dong, T. Wang, T. Wang, M. P. Zaletel, A. Vishwanath, and D. E. Parker, Anomalous Hall crystals in rhombohedral multilayer graphene. II. General mechanism and a minimal model, *Phys. Rev. B* **110**, 205124 (2024), publisher: American Physical Society.

[12] Z. Dong, A. S. Patri, and T. Senthil, Theory of Quantum Anomalous Hall Phases in Pentalayer Rhombohedral Graphene Moiré Structures, *Phys. Rev. Lett.* **133**, 206502 (2024), publisher: American Physical Society.

[13] Z. Dong, A. S. Patri, and T. Senthil, Stability of anomalous Hall crystals in multilayer rhombohedral graphene, *Phys. Rev. B* **110**, 205130 (2024), publisher: American Physical Society.

[14] B. Zhou, H. Yang, and Y.-H. Zhang, Fractional Quantum Anomalous Hall Effect in Rhombohedral Multilayer Graphene in the Moiréless Limit, *Phys. Rev. Lett.* **133**, 206504 (2024), publisher: American Physical Society.

[15] B. Zhou and Y.-H. Zhang, New Classes of Quantum Anomalous Hall Crystals in Multilayer Graphene, *Phys. Rev. Lett.* **135**, 036501 (2025), publisher: American Physical Society.

[16] F. Desrochers, M. R. Hirsbrunner, J. Huxford, A. S. Patri, T. Senthil, and Y. B. Kim, *Elastic Response and Instabilities of Anomalous Hall Crystals* (2025), arXiv:2503.08784 [cond-mat].

[17] Z. Guo and J. Liu, *Correlation stabilized anomalous Hall crystal in bilayer graphene* (2025), arXiv:2409.14658 [cond-mat].

[18] Y. H. Kwan, J. Yu, J. Herzog-Arbeitman, D. K. Efetov, N. Regnault, and B. A. Bernevig, Moiré fractional chern insulators. iii. hartree-fock phase diagram, magic angle regime for chern insulator states, role of moiré potential, and goldstone gaps in rhombohedral graphene superlattices, *Phys. Rev. B* **112**, 075109 (2025).

[19] J. Yu, J. Herzog-Arbeitman, Y. H. Kwan, N. Regnault, and B. A. Bernevig, Moiré fractional chern insulators. iv. fluctuation-driven collapse in multiband exact diagonalization calculations on rhombohedral graphene, *Phys. Rev. B* **112**, 075110 (2025).

[20] B. A. Bernevig and Y. H. Kwan, “berry trashcan” model of interacting electrons in rhombohedral graphene (2025), arXiv:2503.09692.

[21] Z. Lu, T. Han, Y. Yao, A. P. Reddy, J. Yang, J. Seo, K. Watanabe, T. Taniguchi, L. Fu, and L. Ju, Fractional quantum anomalous Hall effect in multilayer graphene, *Nature* **626**, 759 (2024), publisher: Nature Publishing Group.

[22] Z. Lu, T. Han, Y. Yao, Z. Hadjri, J. Yang, J. Seo, L. Shi, S. Ye, K. Watanabe, T. Taniguchi, and L. Ju, Extended quantum anomalous Hall states in graphene/hBN moiré superlattices, *Nature* **637**, 1090 (2025), publisher: Nature Publishing Group.

[23] J. Xie, Z. Huo, X. Lu, Z. Feng, Z. Zhang, W. Wang, Q. Yang, K. Watanabe, T. Taniguchi, K. Liu, Z. Song, X. C. Xie, J. Liu, and X. Lu, Tunable fractional Chern insulators in rhombohedral graphene superlattices, *Nat. Mater.* **24**, 1042 (2025), publisher: Nature Publishing Group.

[24] K. Yang, X. Gao, Y. Wang, T. Zhang, Y. Gao, X. Lu, S. Zhang, J. Liu, P. Gu, Z. Luo, R. Zheng, S. Cao, H. Wang, X. Sun, K. Watanabe, T. Taniguchi, X. Li, J. Zhang, X. Dai, J.-H. Chen, Y. Ye, and Z. Han, Unconventional correlated insulator in CrOCl-interfaced Bernal bilayer graphene, *Nat Commun* **14**, 2136 (2023), publisher: Nature Publishing Group.

[25] J. Sun, S. A. Akbar Ghorashi, K. Watanabe, T. Taniguchi, F. Camino, J. Cano, and X. Du, Signature of Correlated Insulator in Electric Field Controlled Superlattice, *Nano Lett.* **24**, 13600 (2024), publisher: American Chemical Society.

[26] Z. Zhang, J. Xie, W. Zhao, R. Qi, C. Sanborn, S. Wang, S. Kahn, K. Watanabe, T. Taniguchi, A. Zettl, M. Crommie, and F. Wang, Engineering correlated insulators in bilayer graphene with a remote Coulomb superlattice, *Nat. Mater.* **23**, 189 (2024), publisher: Nature Publishing Group.

[27] S. A. A. Ghorashi, A. Dunbrack, A. Abouelkomansan,

J. Sun, X. Du, and J. Cano, Topological and Stacked Flat Bands in Bilayer Graphene with a Superlattice Potential, *Phys. Rev. Lett.* **130**, 196201 (2023), publisher: American Physical Society.

[28] Y. Zeng, T. M. R. Wolf, C. Huang, N. Wei, S. A. A. Ghorashi, A. H. MacDonald, and J. Cano, Gate-tunable topological phases in superlattice modulated bilayer graphene, *Phys. Rev. B* **109**, 195406 (2024), publisher: American Physical Society.

[29] Y. Shi, B. Xie, F. Ren, X. Cai, Z. Guo, Q. Li, X. Lu, N. Regnault, Z. Liu, and J. Liu, Fractional topological states in rhombohedral multilayer graphene modulated by kagome superlattice (2025), arXiv:2502.17320 [cond-mat].

[30] Z. Zhan, Y. Li, and P. A. Pantaleón, Designing band structures by patterned dielectric superlattices, *Phys. Rev. B* **111**, 10.1103/physrevb.111.045148 (2025), publisher: American Physical Society (APS).

[31] P. A. Pantaleón, Z. Zhan, S. E. Morales, and G. G. Naumis, Designing flat bands and pseudo-Landau levels in GaAs with patterned gates, *Phys. Rev. B* **111**, 245303 (2025), publisher: American Physical Society.

[32] T. Cookmeyer and S. Das Sarma, Symmetry breaking in zero-field two-dimensional electron bilayers, *Phys. Rev. B* **109**, 115307 (2024), publisher: American Physical Society.

[33] J. Zhu and S. Das Sarma, Interaction and coherence in two-dimensional bilayers, *Phys. Rev. B* **109**, 085129 (2024), publisher: American Physical Society.

[34] H. C. Po, H. Watanabe, and A. Vishwanath, Fragile topology and wannier obstructions, *Phys. Rev. Lett.* **121**, 126402 (2018).

[35] P. G. Silvestrov and P. Recher, Wigner crystal phases in bilayer graphene, *Phys. Rev. B* **95**, 075438 (2017).

[36] S. Joy and B. Skinner, Wigner crystallization in bernal bilayer graphene, arXiv preprint arXiv:2310.07751 (2023).

[37] E. Aguilar-Méndez, T. Neupert, and G. Wagner, Full, three-quarter, half and quarter wigner crystals in bernal bilayer graphene (2025), arXiv:2505.09685.

[38] X. Zhu, P. B. Littlewood, M. S. Hybertsen, and T. M. Rice, Exciton condensate in semiconductor quantum well structures, *Phys. Rev. Lett.* **74**, 1633 (1995).

[39] B. Seradjeh, J. E. Moore, and M. Franz, Exciton condensation and charge fractionalization in a topological insulator film, *Phys. Rev. Lett.* **103**, 066402 (2009).

[40] D. I. Pikulin and T. Hyart, Interplay of exciton condensation and the quantum spin hall effect in InAs/GaSb bilayers, *Phys. Rev. Lett.* **112**, 176403 (2014).

[41] Q. Zhu, M. W.-Y. Tu, Q. Tong, and W. Yao, Gate tuning from exciton superfluid to quantum anomalous hall in van der waals heterobilayer, *Science Advances* **5**, eaau6120 (2019), <https://www.science.org/doi/pdf/10.1126/sciadv.aau6120>.

[42] Y. Zeng and A. H. MacDonald, Electrically controlled two-dimensional electron-hole fluids, *Phys. Rev. B* **102**, 085154 (2020).

[43] Y. Shao and X. Dai, Quantum oscillations in an excitonic insulating electron-hole bilayer, *Phys. Rev. B* **109**, 155107 (2024).

[44] J. Zhu and S. Das Sarma, Interaction and coherence in two-dimensional bilayers, *Phys. Rev. B* **109**, 085129 (2024).

[45] J. Zhu and S. D. Sarma, 2d bilayer electron-hole superfluidity with unequal and anisotropic masses (2025), arXiv:2508.09982.

[46] X. Lu, S. Zhang, Y. Wang, X. Gao, K. Yang, Z. Guo, Y. Gao, Y. Ye, Z. Han, and J. Liu, Synergistic correlated states and nontrivial topology in coupled graphene-insulator heterostructures, *Nat Commun* **14**, 5550 (2023), publisher: Nature Publishing Group.

[47] Supplemental material for “emergence of topological electronic crystals in bilayer graphene-mott insulator heterostructures” (2025), see Supplemental Material at [URL will be inserted by publisher].

[48] V. Crépel and J. Cano, Efficient Prediction of Superlattice and Anomalous Miniband Topology from Quantum Geometry, *Phys. Rev. X* **15**, 011004 (2025), publisher: American Physical Society.

[49] B. Skinner and B. I. Shklovskii, Anomalously large capacitance of a plane capacitor with a two-dimensional electron gas, *Phys. Rev. B* **82**, 155111 (2010).

[50] J. Topping, On the mutual potential energy of a plane network of doublets, *Proc. R. Soc. Lond. A Math. Phys. Sci.* **114**, 67 (1927).

[51] K. Yang, Z. Xu, Y. Feng, F. Schindler, Y. Xu, Z. Bi, B. A. Bernevig, P. Tang, and C.-X. Liu, Topological minibands and interaction driven quantum anomalous Hall state in topological insulator based moiré heterostructures, *Nat Commun* **15**, 2670 (2024), publisher: Nature Publishing Group.

[52] T. Tan, A. P. Reddy, L. Fu, and T. Devakul, Designing Topology and Fractionalization in Narrow Gap Semiconductor Films via Electrostatic Engineering, *Phys. Rev. Lett.* **133**, 206601 (2024), publisher: American Physical Society.

[53] W. Miao, A. Rashidi, and X. Dai, Artificial moiré engineering for an ideal Bernevig-Hughes-Zhang model, *Phys. Rev. B* **111**, 045113 (2025), publisher: American Physical Society.

[54] K. Yang, Y. Liu, F. Schindler, and C.-X. Liu, Engineering miniband topology via band folding in moiré superlattice materials, *Phys. Rev. B* **111**, L241104 (2025), publisher: American Physical Society.

[55] Y. Liu, A. Aryal, D. Calugaru, Z. Fang, K. Yang, H. Hu, Q. Yan, B. A. Bernevig, and C. xing Liu, “ideal” topological heavy fermion model in two-dimensional moiré heterostructures with type-ii band alignment (2025), arXiv:2507.06168.

[56] Y. Zhang, Y. Gu, H. Weng, K. Jiang, and J. Hu, Mottness in two-dimensional van der waals nb_3X_8 monolayers ($x = Cl, Br$, and I), *Phys. Rev. B* **107**, 035126 (2023).

[57] S. Gao, S. Zhang, C. Wang, S. Yan, X. Han, X. Ji, W. Tao, J. Liu, T. Wang, S. Yuan, G. Qu, Z. Chen, Y. Zhang, J. Huang, M. Pan, S. Peng, Y. Hu, H. Li, Y. Huang, H. Zhou, S. Meng, L. Yang, Z. Wang, Y. Yao, Z. Chen, M. Shi, H. Ding, H. Yang, K. Jiang, Y. Li, H. Lei, Y. Shi, H. Weng, and T. Qian, Discovery of a single-band mott insulator in a van der waals flat-band compound, *Phys. Rev. X* **13**, 041049 (2023).

[58] Q. Yang, M. Wu, J. Duan, Z. Ma, L. Li, Z. Huo, Z. Zhang, K. Watanabe, T. Taniguchi, X. Zhao, Y. Chen, Y. Shi, W. Jiang, K. Liu, and X. Lu, Evidence of mott insulator with thermally induced melting behavior in kagome compound Nb₃Cl₈, *Natl. Sci. Rev.* (2025).

[59] M. Levin and A. Stern, Fractional topological insulators, *Physical review letters* **103**, 196803 (2009).

[60] X.-L. Qi, Generic wave-function description of fractional

quantum anomalous hall states? format? and fractional topological insulators, *Physical review letters* **107**, 126803 (2011).

[61] K. Kang, B. Shen, Y. Qiu, Y. Zeng, Z. Xia, K. Watanabe, T. Taniguchi, J. Shan, and K. F. Mak, Evidence of the fractional quantum spin hall effect in moiré moire2, *Nature* **628**, 522 (2024).

[62] Y.-H. Zhang, Vortex spin liquid with fractional quantum spin hall effect in moiré chern bands, *Physical Review Letters* **133**, 106502 (2024).

[63] C.-M. Jian, M. Cheng, and C. Xu, Minimal fractional topological insulator in half-filled conjugate moiré chern bands, *Physical Review X* **15**, 021063 (2025).

[64] B. Zou, A. Li, and A. H. MacDonald, Valley order in moiré topological insulators (2025), [arXiv:2509.07784](https://arxiv.org/abs/2509.07784).

[65] Y. Zeng and A. H. MacDonald, Strong modulation limit of excitons and trions in moiré materials, *Phys. Rev. B* **106**, 035115 (2022).

[66] D. D. Dai and L. Fu, Strong-coupling phases of trions and excitons in electron-hole bilayers at commensurate densities, *Phys. Rev. Lett.* **132**, 196202 (2024).

[67] P. X. Nguyen, R. Chaturvedi, L. Ma, P. Knuppel, K. Watanabe, T. Taniguchi, K. F. Mak, and J. Shan, An equilibrium trion liquid in atomic double layers, *Science* **390**, 304 (2025).

[68] R. Qi, Q. Li, Z. Zhang, S. Chen, J. Xie, Y. Ou, Z. Cui, D. D. Dai, A. Y. Joe, T. Taniguchi, K. Watanabe, S. Tongay, A. Zettl, L. Fu, and F. Wang, Electrically controlled interlayer trion fluid in electron-hole bilayers, *Science* **390**, 299 (2025).

[69] Z. Wang, R. Song, Y. Jiang, Q. Sun, M. Zhao, L. Yin, J. Shen, and C. Gao, Intrinsic heavy wigner crystal forged by transferred 4f electrons, *Phys. Rev. Lett.* **135**, 266502 (2025).

[70] The related experimental manuscript is in preparation. (2025).

END MATTER

To minimize finite size effects and enable a controlled comparison of total energies among electronic crystal states with different lattice geometries, we perform self consistent calculations on a sequence of increasingly dense (n_k, n_k) k -meshes. For each mesh we evaluate the condensation energy e per electron-hole pair, $e(n_k)$. Since the dominant discretization error is expected to scale with the inverse number of sampled k points, $N_k = n_k^2$, we extrapolate to the thermodynamic limit by fitting $e(n_k)$ linearly in $1/n_k^2$, $e(n_k) = e(n_k \rightarrow \infty) + \frac{a}{n_k^2}$. The intercept $e(n_k \rightarrow \infty)$ is taken as the infinite k -mesh estimate, and the same extrapolation protocol is applied to all candidate geometries to ensure an unbiased energy comparison. The condensation energy in the thermal dynamic limit for the case studied in Fig. 3 is shown in Fig. 5.

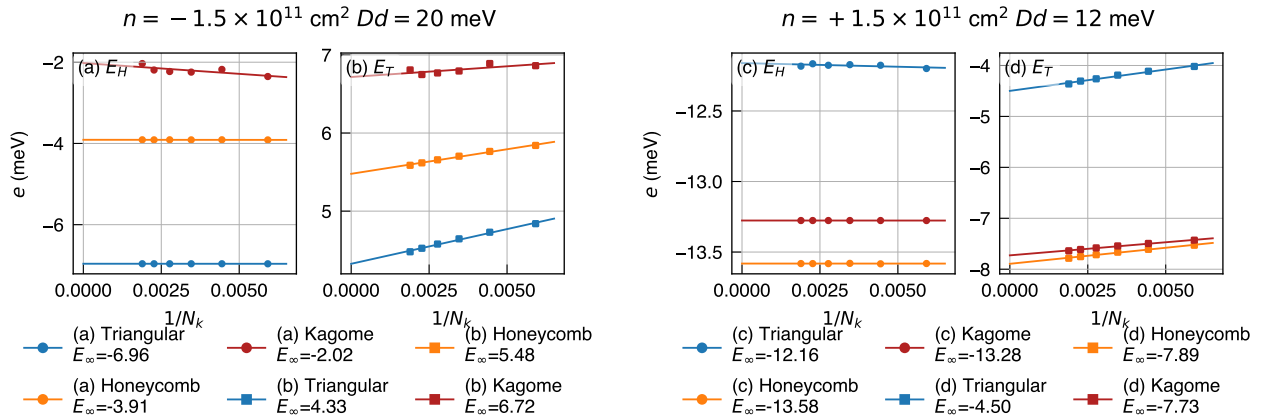


FIG. 5. Finite size scaling of the Hartree energy and total energy per electron hole pair for the case shown in Fig. 3, computed at different k -meshes. Panels (a,b) correspond to charge transfer from BLG to the MI ($n < 0$), and (c,d) to the reverse direction ($n > 0$). Energies are plotted as functions of $1/N_k$, where N_k is the total number of k points. Solid lines indicate linear extrapolations to the thermodynamic limit, with extrapolated values labeled in the legend.